A new characterisation method for rubber

T Guélon, Evelyne Toussaint, Jean-Benoit Le Cam, N Promma, Michel Grediac

A new characterisation method for rubber

T. Guélon[(a)], E. Toussaint[(a)], J.-B. Le Cam[(a)], N. Promma[(a)] and M. Grédiac[(a)]

(a) Laboratoire de Mécanique et Ingénieries, Institut Français de Mécanique Avancée - Université Blaise Pascal Clermont II, Campus des Cézeaux, BP 265, 63175 Aubière Cedex, France.

Abstract

This paper deals with the mechanical characterisation of elastomeric materials. An original method is proposed to identity the material parameters. It consists of performing only one heterogeneous mechanical test, measuring the displacement/strain field using suitable Digital Image Correlation software and applying an inverse method, namely the Virtual Fields Method, to process the resulting displacement/strain maps. For this purpose, a new apparatus is designed to be adapted to a conventional tensile machine. This apparatus enables us to obtain simultaneously uniaxial tension, pure shear and equibiaxial tension, using only one sample. The heterogeneity of the kinematic fields induced by the test is first discussed in relation to two criteria. The main features of the identification method are then presented, and results provided by a test performed on an elastomeric material are discussed in the context of hyperelasticity.

Keywords

test-induced heterogeneity, hyperelasticity, inverse problem, identification

1-Introduction

The behaviour of rubber-like materials is generally modelled in the framework of hyperelasticity. Numerous constitutive relations are available in the literature and have recently been compared in the work of Marckmann et al [1]. However, the identification of the material parameters that govern the constitutive equations is still a difficult task. Classically, three homogeneous tests are considered to identify constitutive parameters, namely uniaxial tensile (UT), pure shear (PS) and equibiaxial tensile (ET) [2, 3, 4]. In practice, the constitutive parameters that are identified with these three types of test differ from one test to another. A trade-off between these three sets of values has to be found to obtain parameters which can be considered as intrinsic. This approach derives from the strong assumption of homogeneity of the kinematic fields induced by each test. Moreover, the sample geometry is different for each homogeneous test.

In the present work, a new approach is developed. It consists of performing only one heterogeneous test, which simultaneously generates the three types of strain states mentioned above as well as the intermediary states. With regard to a recent study by the authors [5], the challenge here resides in using a conventional uniaxial tensile machine to generate a heterogeneous strain state. For this purpose, the sample geometry and loading conditions are defined beforehand by numerical investigations. To generate UT, PS and ET, a new apparatus is designed to be adapted to the uniaxial testing machine. Two specific criteria are defined to discuss the heterogeneity induced by the test. From an experimental point of view, kinematic fields are provided by a Digital Image Correlation (DIC) code suitable for large strains: CORRELI^{LMT} [6]. Finally, the constitutive parameters are identified using an inverse method, namely the Virtual Fields Method, which is extended to the case of finite deformations.

2-Choice of sample geometry and loading conditions

As mentioned above, the aim of the present work is to perform a heterogeneous test that combines UT, PS and ET using a conventional tensile machine. For this purpose, a numerical approach is used to choose the sample geometry and loading conditions, in order to generate sufficient heterogeneity of the kinematic fields. First, criteria used to estimate Test-Induced Heterogeneity (TIH) are defined, and then the kinematic fields obtained from the chosen sample geometry and the applied loading conditions are presented.

2-1 Test-Induced Heterogeneity

The heterogeneity induced by the test is analysed using the diagram in Fig. 1. This diagram allows us to determine the loading condition applied at each material point of the kinematic field from the corresponding values of I_1 and I_2. I_1 and I_2 are the first and second invariants of the right Cauchy-Green tensor **C** [7]:

$$\left.\begin{aligned} I_1 &= \lambda_1^2 + \lambda_2^2 + \lambda_3^2 \\ I_2 &= \lambda_1^2\lambda_2^2 + \lambda_2^2\lambda_3^2 + \lambda_3^2\lambda_1^2 \end{aligned}\right\} \quad (1)$$

where, λ_1, λ_2 and λ_3 are the eigenvalues of the deformation gradient tensor **F**.

Here, three curves corresponding to UT, PS, and ET are plotted. Note that all the loading paths are located between UT and ET [2]. The localisation of any point in this diagram indicates the corresponding loading condition: it can be either one of the three previous loadings or a combination of two of them.

In the present work, we propose to characterize TIH in relation to two criteria:

- Criterion 1: the test has to generate the three homogeneous loading conditions, namely UT, PS and ET ;

- Criterion 2: for each loading condition, i.e. UT, PS and ET, a relative distribution of the maximum principal stretch ratio (defined as the ratio between actual and initial lengths) must be observed. This relative distribution must be sufficiently wide, considering the chosen constitutive equations and their fields of validity. This criterion is discussed in relation to two diagrams which are deduced from that of Fig. 1. They are more precisely detailed in Section *2-2*.

In the following, these criteria are used to choose both sample geometry and loading conditions.

2-2 Sample geometry and loading conditions

The TIH depends on both the sample geometry and the loading conditions. As a uniaxial testing machine is used in the present study, a change in geometry (for instance by adding notches [8]) could be considered to generate heterogeneity in the kinematic fields. However, contrary to most materials, the strain state obtained in an elastomer under large deformations tends to be homogeneous, i.e. UT, whatever the sample geometry. Even if PS and UT can be easily obtained by adding holes or notches, biaxial loading conditions are necessary to generate ET. For this purpose, numerical investigations are carried out to choose both sample geometry and biaxial loading conditions that generate a high heterogeneity level. Fig. 2 presents the sample geometry chosen and the loading conditions applied. The sample geometry, which corresponds to a three-branch sample, is 2 mm thick and 60 mm high, and the branches are 20 mm in width. The bottom branch is clamped; the loading is carried out by applying prescribed displacement along the axis of the two other perpendicular branches.

A Finite Element Analysis is first performed using the Ansys 10.0 package to investigate the TIH. To ensure the assumption of incompressibility, element type Plane182 is used. The mesh is composed of 640 elements. This number of elements is close to the number of measurement points obtained experimentally with a camera observing the sample surface. Further

information about experimental considerations is given in section 5. Material behaviour is assumed to be modelled in the framework of hyperelasticity using the strain energy density proposed by Mooney [9], written as:

$$W = C_1(I_1-3) + C_2(I_2-3) \qquad (2)$$

where C_1 and C_2 are the material parameters. Their values are chosen as equal to 0.4 MPa and 0.04 MPa, respectively, which are typical values for carbon black filled natural rubber. The results of the numerical simulations of the mechanical test are discussed in relation to the abovementioned multi-criteria analysis. Fig. 3(a) presents the TIH in the (I_1-I_2) plane. The localisation (Fig. 3(b)) and the corresponding maximum principal elongation (Fig. 3(c)) of each loading case at the sample surface are deduced from Fig. 3(a). Global stretch ratios (defined as the ratio between actual and initial sample lengths) of 1.71 and 1.42 are chosen for the horizontal and the vertical axes, respectively.

As shown in these figures, each of the three homogeneous tests, i.e. UT, PS and ET are satisfactorily represented and distributed. Here, the equivalent maximum stretch ratio is higher for UT than for PS and ET. This is explained by the fact that PS and ET are obtained by the extension of the branches. Fig. 3(b) and Fig. 3(c) are obtained from Fig. 3(a) and from the sample mesh. Fig. 3(b) shows the localisation of each loading case. As expected, UT (red) is located in the branches, ET (blue) is located at the sample centre and PS(green) is located between the other loading cases (criterion 1). Fig. 3(c) presents the maximum principal stretch ratio at each Finite Element. Here, each loading case is satisfactorily represented in terms of distribution of the maximum principal stretch ratio (criterion 2). It is to be noted that the colour scale is obtained for each case from the results presented in Fig. 3(a). For instance, the colour of a point located between two curves is obtained by a weighted average of the two colour scales, the weights being inversely proportional to the distances between this point and the two curves.

With regard to the previous analysis, TIH satisfies the two criteria presented above.

3-Experimental set-up

In the previous section, the sample geometry and the loading conditions applied were numerically validated in terms of TIH. Here, this configuration is used to perform the test with a conventional uniaxial testing machine. To impose a biaxial loading condition, a new apparatus is designed. It is presented below.

3-1 Modification of the conventional uniaxial testing machine

The tests are carried out with a MTS 858 Elastomer Test System testing machine. This testing machine is presented in Fig. 4. Its loading capacity is 15 kN and the loading cell is 1 kN. In order to apply biaxial loading, i.e. to generate ET at the sample centre, a new tensile apparatus is designed to be adapted to the uniaxial tensile machine. As shown in the figure, it is mounted on the left testing machine column. Fig. 5 presents a photo (Fig. 5(a)) and a schematic view (Fig. 5(b)) of the apparatus. It is composed of four parts:

(i) part A allows the apparatus to be fixed to one of the two columns;
(ii) part B is a grip in which the horizontal branch of the sample is fixed;
(iii) part C corresponds to a helical slide which ensures that the horizontal branch of the sample is stretched;
(iv) part D is a ruler used to measure the horizontal displacement of the grip.

In practise, the two vertical branches of the sample are fastened to the grips of the conventional testing machine, then the branch perpendicular to the previous ones is fastened to the apparatus grip.

3-2 Measurement of the displacement fields

Digital Image Correlation (DIC) is used to measure the displacement field on the sample surface [10]. DIC is a full-field measurement technique developed at the beginning of the 1980s [11, 12]. This method consists of matching, before and after displacement, the brindled pattern in a physical part of the observed surface of the specimen, called Region Of Interest (ROI). For this purpose, images are shot with a cooled 12-bit dynamic CCD camera with 1376 x 1040 square pixels, and CORRELI^{LMT} software is used. To determine the displacement field of a given image with respect to a reference image, one considers a set of sub-images (*i.e.*, a square region that contains $N \times N$ pixels). This set is referred to as "Zone of Interest" (ZOI). A suitable correlation function is used to calculate the displacement of the centre of a given ZOI between two images captured at different stages of an experiment. A fast Fourier transform (FFT) approach is implemented in CORRELI^{LMT} software to evaluate the cross-correlation function. To improve image contrast, white paint is sprayed on the sample surface before testing. Fig. 6 presents a histogram of the grey levels of the sample surface. The Gaussian-shaped distribution obtained allows us to perform the image correlation satisfactorily.

The DIC technique is well-suited for measuring large strains [13] and has already been used in the case of elastomeric materials [4, 14]. For this purpose, a multi-scale algorithm is used in CORRELI^{LMT} software to improve the spatial resolution (i.e. to decrease the ZOI size), yet allowing for a large displacement between two consecutive images [15]. In the present work, special attention is paid to the choice of the size of the sub-images or ZOIs that define the ROI. Here, the size of the ZOI (N) is equal to 16 pixels with a shift (⍰P) of 16 pixels. This parameter characterises the "measurement grid".

4-Identification of the material parameters

This section presents the method used to identify the material parameters of a given model from one heterogeneous test. It must be emphasised that no closed-form solution generally

exists for such a problem, thereby meaning that no simple relation between local measurements, load, specimen geometry and unknown parameters is available. Extracting constitutive parameters in this case is a major issue which must be tackled using relevant tools. Various methods have been proposed in the literature in the recent past to solve this type of problem [16]. Among these methods, the so-called Virtual Fields Method (VFM) [17, 18] has recently shown strong promise for characterising elastomeric materials within the context of large deformations. Full details can be found in Ref. [5], so only the main steps of the VFM are recalled here.

The VFM relies on the Principle of Virtual Work (PVW), which can be regarded as the global equilibrium of the specimen under study or the weak form of the local equilibrium equations [19]. In the case of large deformations, assuming a plane state of stress and neglecting body forces such as weight, the PVW can be written as follows [7]:

 K. A. (3)

where Π is the first Piola-Kirchhoff stress tensor (PK1), the X_is are the Lagrangian coordinates, U^* is a kinematically admissible virtual field, S_0 is the surface of the specimen in the initial configuration, ∂S_0 is the boundary of S_0 and n is the unit vector perpendicular to this boundary. In is worth noting that Equation (3) is valid for any kinematically virtual field [18]. This important property is the foundation of the VFM, which comprises two main stages.

Stage 1: The first stage consists of expressing the stress components as functions of actual strain components or any other suitable kinematic quantity. In the present case of hyperelasticity, invariants I_1 and I_2 of the right Cauchy-Green tensor **C** are the relevant quantities (see Section 2.1 above). This leads to the following equation:

 K. A. (4)

where A and B are quantities depending on the components of the deformation gradient tensor F (see appendix A). The right-hand side of this equation is the virtual work of the external load. This is generally known since both the applied load and the virtual field U^* are known, as explained in more detail below. Interestingly, the above equation is linear with respect to the unknown parameters C_1 and C_2. Consequently, if the integrands on the right-hand side of Equation (4) are assumed to be known, one obtains a linear equation where C_1 and C_2 are the unknowns. In the integrands above, there are two types of term: A and B on the one hand, and $\frac{\partial U^*}{\partial X}$ on the other. A and B are directly deduced from the full-field measurements, whereas $\frac{\partial U^*}{\partial X}$ is derived from the virtual field U^*. This remark directly leads to the second stage of the procedure.

Stage 2: The second stage consists of choosing two different kinematically admissible virtual fields and writing Equation (4) with each of these two fields. This is valid since the PVW is valid for any kinematically admissible virtual field, as recalled above. Since actual strain fields are heterogeneous, this leads to two independent equations where C_1 and C_2 are unknown. Note that heterogeneity is here a requirement whereas it is considered as a drawback in the classical identification procedures based on the homogeneity of strain fields. Finally, these two unknowns are obtained simply by inverting the linear system.

Choosing the two virtual fields is a key issue in the method. It is performed using relevant numerical tools in the case of small deformations and elasticity [20]. In the present case of large deformations and hyperelasticity, it was decided to use the following heuristic method. A large number of virtual fields is first randomly generated (3000 in practice, this number being a trade-off between computing time, memory size and the quality of the results

obtained). The set of two virtual fields that leads to the best conditioning of the linear system (assessed with the condition number) is finally chosen for identification purposes. The reason is that these virtual fields provide parameters which are less sensitive to noisy data. Finally, it must be pointed out that the virtual fields are defined here piecewise [21] because of the particular shape of the specimen. Four sub-regions are used to mesh the specimen because of this particular shape. The virtual displacement defined in each of the four sub-regions is described by polynomial shape functions multiplied by the virtual displacement of the nodes defining the corners of the sub-regions. These shape functions are similar to those employed in the Finite Element method [22].

Fig. 7 presents an example of optimised initial fields used for identifying C_1 and C_2 at the maximum global stretch ratios.

5-Results

5-1 Experimental kinematic fields

The biaxial tensile test is carried out by applying a 25 mm displacement along both the *x*- and *y*- directions shown in Figure 2. The corresponding global stretch ratios are respectively 1.71 and 1.42. In order to avoid the well-known phenomenon of stress accommodation [23,24,25] over the first mechanical cycles, three cycles are first carried out with the same stretch ratio, thereby partially stabilising the mechanical response of the specimen. Images are stored for every 1 mm of prescribed displacement in both directions. The material considered here is carbon black filled natural rubber. Its composition and some of its mechanical properties are given in Tab. 1.

Fig. 8(a) and Fig. 8(b) present a typical view of the horizontal and vertical displacement fields obtained for the maximum prescribed global stretch ratios. Then the four components of the gradient displacement involved in Equation 4 are obtained by spatially differentiating the

displacement fields. A centred finite difference scheme is used for this purpose. It is to be noted that for the Finite Element simulation, gradient displacements are directly given by Ansys software. In the present case, 740 experimental points are processed. This number is close to the number of elements used for numerical simulations and makes it easier to compare numerical and experimental TIH visualisations (see Fig. 3 and Fig. 9). Fig. 9(a) shows the distribution of loading cases in the I_1-I_2 plane. As forecast by the numerical investigations, the strain states of the three homogeneous tests (UT, PS and ET) are represented and the equivalent maximum stretch ratio is higher for UT than for PS and ET. Fig. 9(b) and Fig. 9(c) present the localisation of each loading case and the maximum principal stretch ratio for each ZOI, respectively. As expected, UT (red) is located in the branches, ET (blue) is located at the sample centre and PS (green) is located between the two other loading cases. Here, each loading case is satisfactorily represented in terms of maximum stretch ratio distribution. With regard to the previous analysis and numerical prediction, the TIH satisfies the two criteria used to define a sufficient level of heterogeneity. However, some points in Fig. 9(a) are more scattered than in Fig. 3(a). These points, circled in Fig. 9(a), correspond to the zones circled in Fig. 9(b) and Fig. 9(c). As shown in these figures, they correspond to points located at the border of the sample, i.e. in zones for which there are insufficient measurement points to obtain an efficient image correlation.

To summarize, these experimental results are in close agreement with the numerical prediction in terms of TIH.

5-2 Identification results

Identification results are presented in Fig. 10 for each step of the loading. This step is equal to 1 mm along both the *x*- and *y*- directions. The ZOIs that are considered as not being valid in terms of measurement quality (see comment in Section 5-1- above) are not taken into account by the identification procedure. C_1 and C_2 are calculated at each loading step. The horizontal

axis in Fig. 10 corresponds to the global stretch ratio imposed along the *y*- direction. Apart from stretch ratios inferior to 1.05, both C_1 and C_2 remain approximately constant while the global stretch ratio increases, thereby showing that the Mooney model used here correctly describes the actual mechanical response of the specimen. The mean values of C_1 and C_2 deduced from these curves are 0.509 MPa and 0.012 MPa, respectively. These values are acceptable with regard to thermodynamic considerations (see Ref. [26]). It should be noted that only the loading steps corresponding to a global stretch ratio along the *y*- direction ranging between 1.05 and 1.42 are considered here. In fact, identifying C_1 and C_2 in the low stretch ratio domain leads to unreliable results. This is clearly highlighted by plotting the reduced nominal stress as defined in Ref. [9] vs. the stretch ratio for UT, PS and ET loading cases. In this diagram, the value of C_1 and C_2 can only be identified from the linear part of the curve. For low stretch ratios, the relationship between the reduced nominal stress and the stretch ratio does not change linearly and the values of C_1 and C_2 are not correct.

Conclusion

The aim of the present paper is to propose an alternative to the classic method for identifying the constitutive parameters of rubber. For this purpose, only one heterogeneous test is performed. Sample geometry and loading conditions are chosen using numerical simulations in order to involve UT, PS and ET at the sample surface. The test-induced heterogeneity is discussed in relation to two criteria. To perform the heterogeneous test, a new apparatus is designed and is adapted to a conventional tensile machine. Displacement fields are measured on the specimen surface using the DIC technique. Unknown constitutive parameters are then deduced from these fields using a suitable identification procedure: the Virtual Fields Method extended to hyperelasticity. An interesting perspective would be to identify parameters governing more complicated constitutive models. For instance, it could be interesting to take

into account the significant change in volume observed under extension in such a material [27].

Acknowledgements

The support of this research by the "Agence Nationale pour la Recherche" is gratefully acknowledged (PHOTOFIT project).

Dr Xavier Balandraud is gratefully thanked for his helpful contribution.

Appendix A

The A_{ij} components are defined as follows:

$$A_{11}=\frac{2}{D}\left[\left(\lambda_1-\lambda_3\right)\left(\lambda_1^2F_{12}-PF_{11}\right)+\left(\lambda_2-\lambda_3\right)\left(\lambda_2^2F_{22}-PF_{21}\right)\right]$$

$$A_{12}=\frac{2}{D}\left[\left(\lambda_1-\lambda_3\right)\left(\lambda_1^2F_{11}-PF_{12}\right)+\left(\lambda_2-\lambda_3\right)\left(\lambda_2^2F_{21}-PF_{22}\right)\right]$$

$$A_{21}=\frac{2}{D}\left[\left(\lambda_1-\lambda_3\right)\left(\lambda_2^2F_{12}-PF_{11}\right)+\left(\lambda_1-\lambda_3\right)\left(\lambda_2^2F_{22}-PF_{21}\right)\right]$$

$$A_{22}=\frac{2}{D}\left[\left(\lambda_1-\lambda_3\right)\left(\lambda_2^2F_{11}-PF_{12}\right)+\left(\lambda_2-\lambda_3\right)\left(\lambda_2^2F_{21}-PF_{22}\right)\right]$$

with $D=F_{11}F_{22}-F_{21}F_{12}$

The B_{ij} components are defined as follows:

$$B_{11}=\frac{2}{D}\left[\left(\frac{1}{\lambda_1}-\frac{1}{\lambda_3}\right)\left(\lambda_1^2F_{12}-PF_{11}\right)+\left(\frac{1}{\lambda_2}-\frac{1}{\lambda_3}\right)\left(\lambda_2^2F_{22}-PF_{21}\right)\right]$$

$$B_{12}=\frac{2}{D}\left[\left(\frac{1}{\lambda_1}-\frac{1}{\lambda_3}\right)\left(\lambda_1^2F_{11}-PF_{12}\right)+\left(\frac{1}{\lambda_2}-\frac{1}{\lambda_3}\right)\left(\lambda_2^2F_{21}-PF_{22}\right)\right]$$

$$B_{21}=\frac{2}{D}\left[\left(\frac{1}{\lambda_1}-\frac{1}{\lambda_3}\right)\left(\lambda_2^2F_{12}-PF_{11}\right)+\left(\frac{1}{\lambda_1}-\frac{1}{\lambda_3}\right)\left(\lambda_2^2F_{22}-PF_{21}\right)\right]$$

$$B_{22}=\frac{2}{D}\left[\left(\frac{1}{\lambda_1}-\frac{1}{\lambda_3}\right)\left(\lambda_2^2F_{11}-PF_{12}\right)+\left(\frac{1}{\lambda_2}-\frac{1}{\lambda_3}\right)\left(\lambda_2^2F_{21}-PF_{22}\right)\right]$$

P is the transition matrix between the Cauchy stress tensor expressed in any 1-2 basis and its eigenbasis.

References

[1] G. Marckmann, E. Verron, Comparison of hyperelastic models for rubberlike materials, *Rubber Chem. Technol.*, 79 (2006) 835-858.

[2] C. G'Sell, A. Coupard, Génie Mécanique des caoutchoucs et des élastomères thermoplastiques, Apollor, 1994.

[3] I. M. Ward, D. W. Hadley, An Introduction to the Mechanical Properties of Solid Polymers, 2nd Edition, John Wiley and Sons Ltd, New-York, 1993.

[4] M. Sasso, G. Palmieri, G. Chiappini, D. Amodio , Characterisation of hyperelastic rubber-like materials by biaxial and uniaxial stretching tests based on optical methods, *Polymer Testing*, 27 (2008), 995-1004

[5] N. Promma, B. Raka, M. Grédiac, E. Toussaint, J.-B. Le Cam, X. Balandraud, F. Hild, Application of the virtual fields method to mechanical characterisation of elastomeric materials, *Int. J. Solids Struct.*, 46 (2009), 698-715

[6] F. Hild, Correli^{LMT}: a software for displacement field measurements by digital image correlation, internal report n° 254, 2002.

[7] G. A. Holzapfel, Nonlinear Solid Mechanics. A continuum approach for engineering, J. Wiley and Sons, Chichester, 2000.

[8] M. Meuwissen, C. Oomens, F. Baaijens, R. Petterson, J. Janssen, Determination of the elasto-plastic properties of aluminium using a mixed numerical-experimental method, *J Mater. Process. Tech.* 75 (1998) 204–211.

[9] M. Mooney, A theory of large elastic deformation, *J. Appl. Phys.* 11 (1940) 582–592.

[10] Pan Bing, Xie Hui-min, Hua Tao, Anand Asundi, Measurement of coefficient of thermal expansion of films using digital image correlation method, *Polymer Testing*, 28 (2009), 75-83.

[11] M.A. Sutton, W.J. Wolters, W.H. Peters, W.F. Ranson and S.R. McNeil, Determination of displacements using an improved digital correlation method, *Image Vision Comput* 1**,** 3 (1983), 133–139.

[12] M.A. Sutton, W.J. Wolters, W.H. Peters, W.F. Ranson and S.R. McNeil, Application of an optimised digital image correlation method to planar deformation analysis, *Image Vision Comput* 4, 3 (1986), 143–151.

[13] F. Lagattu, J. Brillaud, M.-C. Lafarie-Frenot, High strain gradient measurements by using digital image correlation technique, *Materials Characterisation* 53, (2004), 17-28

[14] L. Chevalier, S. Calloch, F. Hild, Y. Marco, Digital image correlation used to analyze the multiaxial behavior of rubber-like materials, *Eur. J of Mech. A-Solid* 20, 2 (2001) 169–187.

[15] F. Hild, B. Raka, M. Baudequin, S. Roux and F. Cantelaube, Multi-scale displacement field measurements of compressed mineral wool samples by digital image correlation, Appl Opt. 32 (2002), 6815–6828.

[16] S. Avril, M. Bonnet, A.S. Bretelle, M. Grédiac, F. Hild, P. Ienny, F. Latourte, D. Lemosse, S. Pagano, S. Pagnacco, F. Pierron, Overview of identification methods of mechanical parameters based on full-field measurements, Experimental Mechanics, 48, 4 (2008), 381-402

[17] M. Grédiac, Principe des travaux virtuels et identification. Principle of virtual work and identification, Comptes Rendus de l'Académie des Sciences (1989) 1–5 Gauthier-Villars. In French with abridged English version.

[18] M. Grédiac, F. Pierron, S. Avril, E. Toussaint, The virtual fields method for extracting constitutive parameters from full-field measurements: a review, *Strain* 42 (2006) 233–253.

[19] C. L. Dym, I. H. Shames, Solid Mechanics A Variational Approach, McGraw-Hill Book Company, 1973

[20] S. Avril, M. Grédiac, F. Pierron, Sensitivity of the virtual fields method to noisy data, Computational Mechanics, 34 (2004), 439-452

[21] E. Toussaint, M. Grédiac, F. Pierron, The virtual fields method with piecewise virtual fields, *Int. J Mech. Sci.* 48 (2006) ,256–264.

[22] O. C. Zienkiewicz, R. L. Taylor, The Finite Element Method, sixth edition, 2005

[23] L. Mullins, Effect of stretching on the properties of rubber, *Rubber Chem. Technol.* 21 (1948) 281–300.

[24] L. Meunier, G. Chagnon, D. Favier, L. Orgéas, P. Vacher , Mechanical experimental characterisation and numerical modelling of an unfilled silicone rubber, *Polymer Testing*, 27 (2008), 765-777.

[25] N. Godin, S. Chaki, J. Courbon, S. Deschanel, S. Gillet, B. Gautier , Acoustic emission potentialities for characterisation of Mullins effect in natural rubber materials filled with carbon black, *Polymer Testing*, 28 (2009), 103- 105

[26] J. Ball, Convexity conditions and existence theorems in nonlinear elasticity, *Arch. for Ration. Mech. An.* 63 (1977) 337–403.

[27] J.-B. Le Cam, E. Toussaint, Volume variation in stretched natural rubber: competition between cavitation and stress-induced crystallisation, *Macromolecules*, 41, 20 (2008), 7579–7583.

Figure captions:

Fig. 1: Three basic loading cases

Fig. 2: Sample geometry and loading conditions

Fig. 3: Numerical TIH visualisation (a) Loading cases in the (I_1-I_2) plane (b) Localisation of loading cases (c) Maximum value of the principal stretch ratio

Fig. 4: Experimental set-up

Fig. 5: Proposed apparatus (a) Four main components (b) Schematic view (dimensions in mm)

Fig. 6: Histogram of grey levels

Fig. 7: Example of two optimised virtual fields (dotted line) used for identifying C_1 and C_2. The virtually deformed fields are superimposed on the undeformed virtual mesh (solid line).

Fig. 8: Displacement fields (a) Displacement field U (b) Displacement field V

Fig. 9: Experimental TIH visualisation (a) Loading cases in the (I_1-I_2) plane (b) Localisation of the loading cases (c) Maximum value of the principal stretch ratio

Fig. 10: Identification of the material parameters (a) C_1 (b) C_2

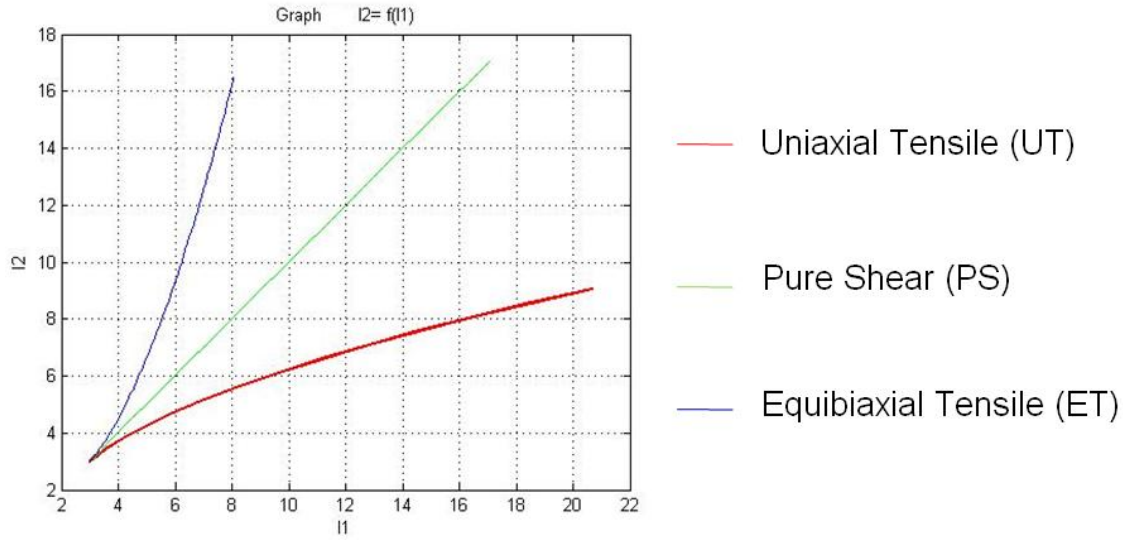

Figure 1 : Three basic loading cases

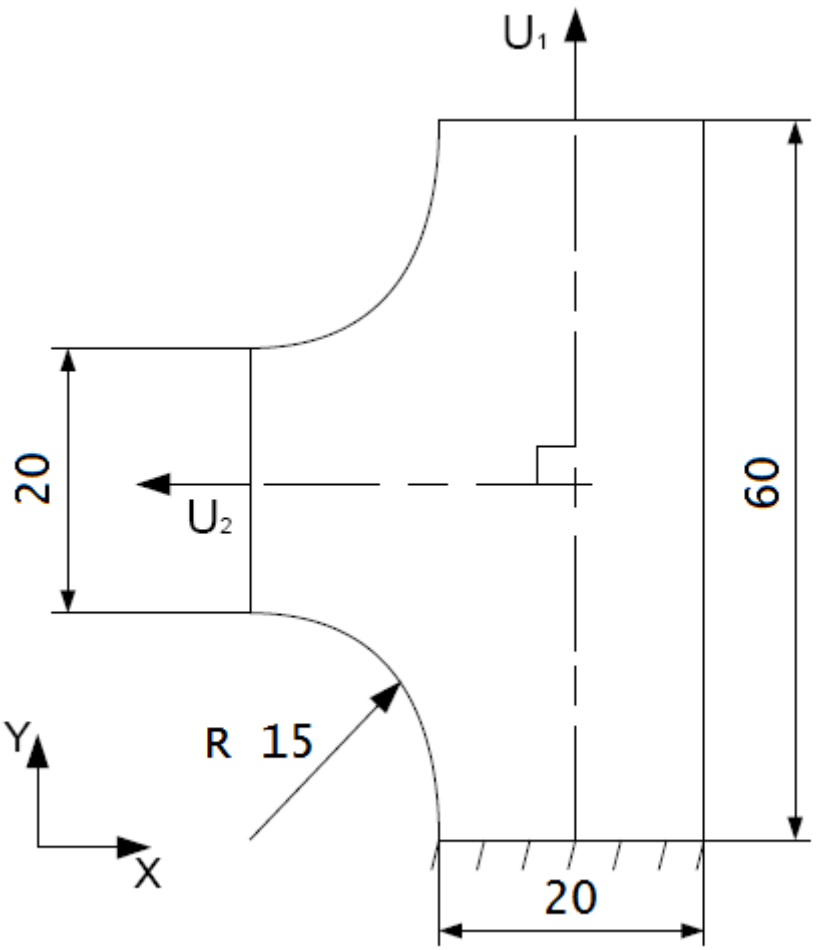

Figure 2 : Sample geometry and loading conditions

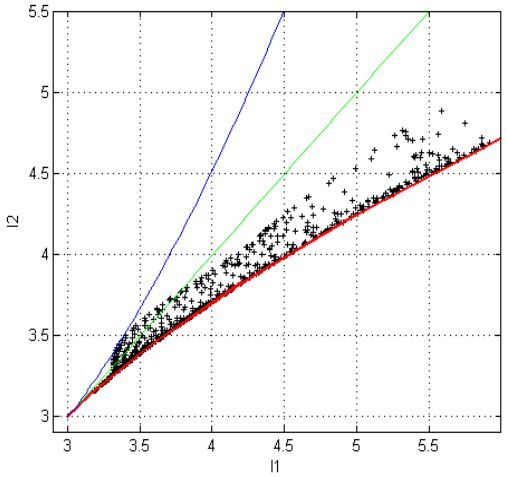

(a)

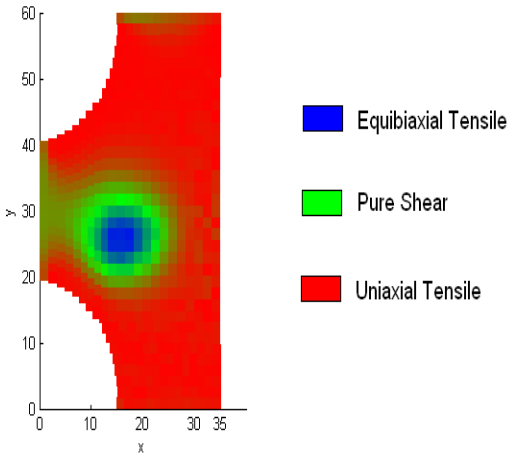

(b)

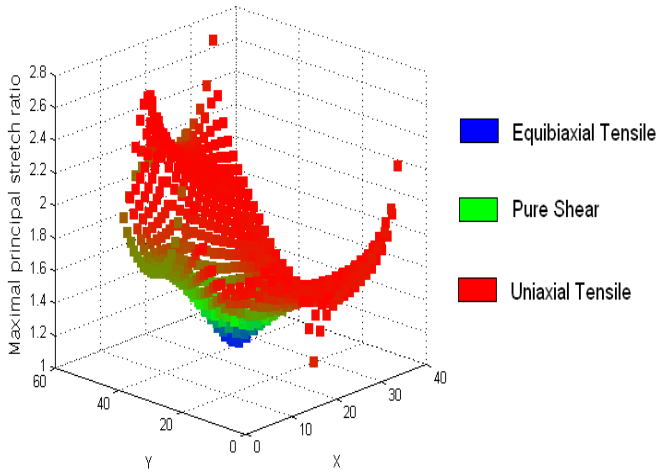

(c)

Figure 3 : Numerical TIH visualisation (a) Loading cases in the (I_1-I_2) plane (b) Localisation of loading cases (c) Maximum value of the principal stretch ratio.

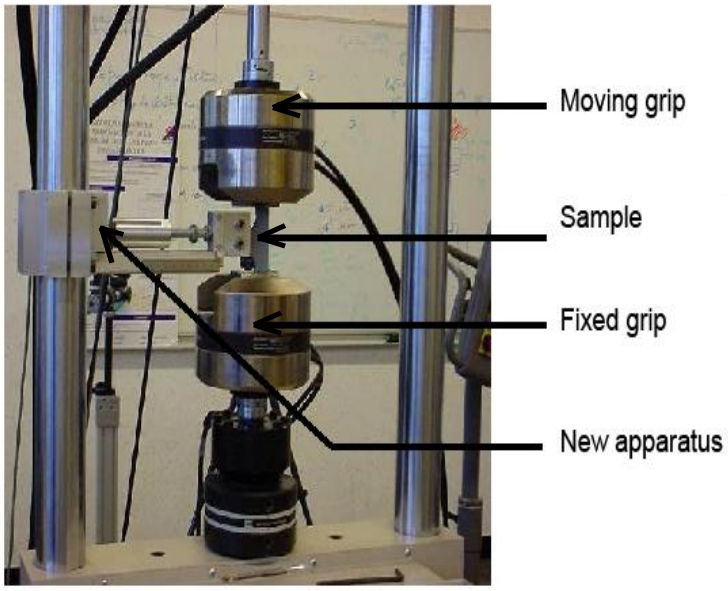

Figure 4 : Experimental set-up

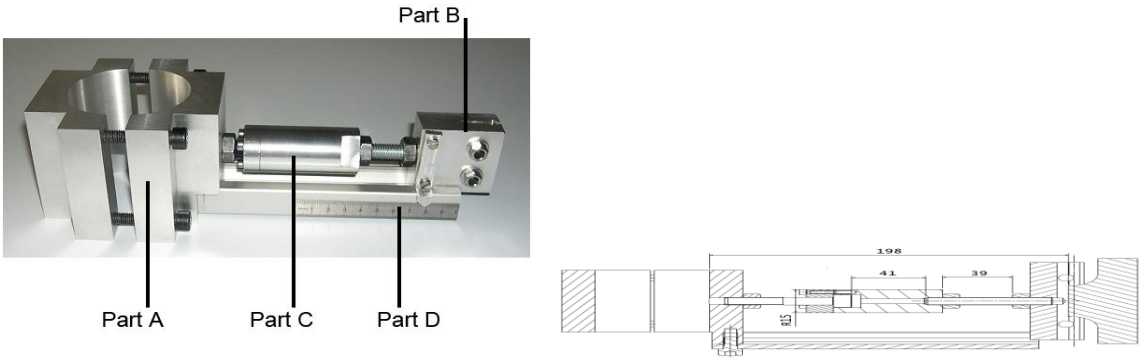

(a) (b)

Figure 5 : Proposed apparatus (a) Four main components (b) Schematic view (dimensions in mm)

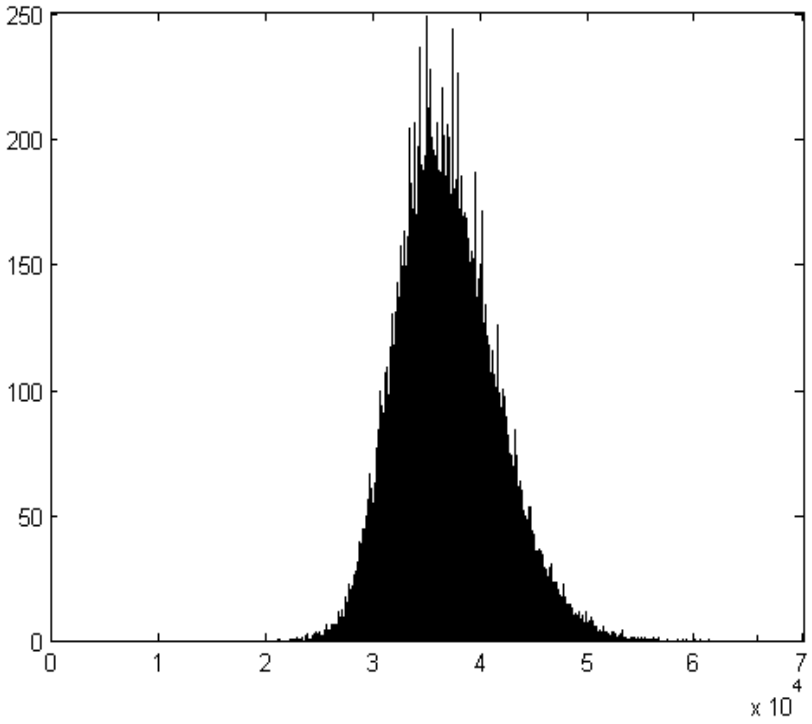

Figure 6 : Histogram of grey levels

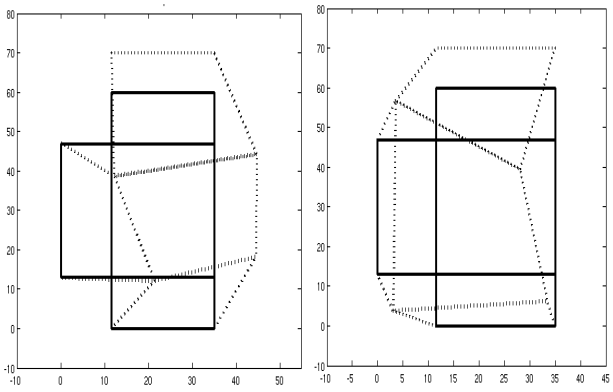

Figure 7 : Example of two optimised virtual fields (dotted line) used for identifying C_1 and C_2 . The virtually deformed fields are superimposed on the undeformed virtual mesh (solid line).

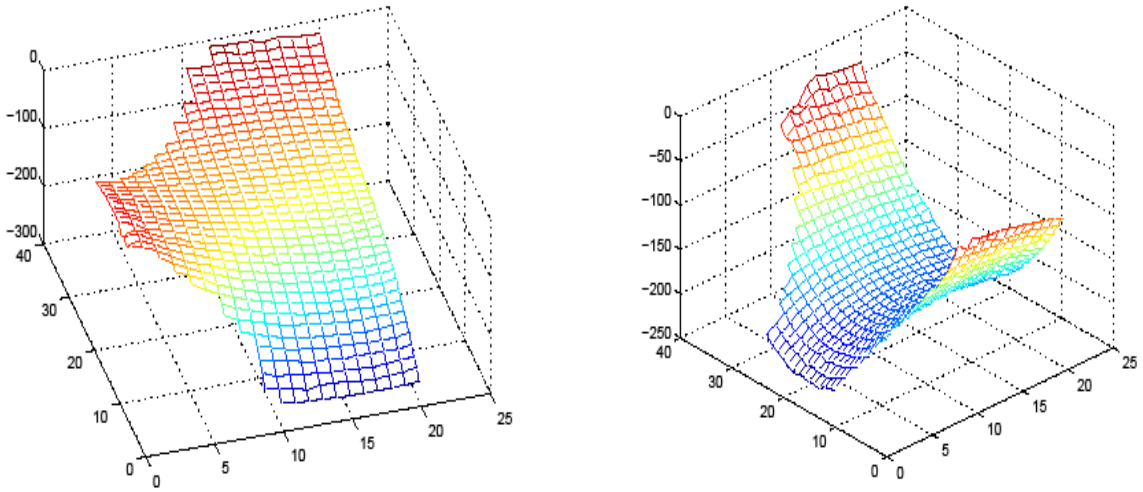

(a) (b)

Figure 8 : Displacement fields (a) Displacement field U (b) Displacement field V

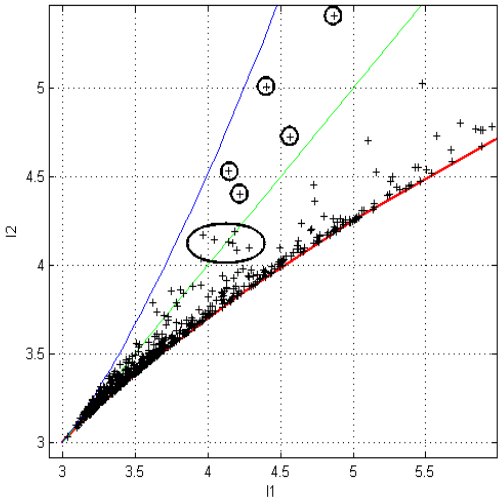

(a)

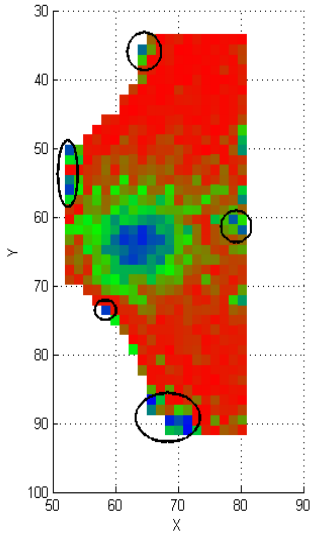

(b)

(c)

(c)

Figure 9 : Experimental TIH visualisation (a) Loading cases in the (I_1-I_2) plane ; (b) Localisation of the loading cases ; (c) Maximum value of the principal stretch ratio

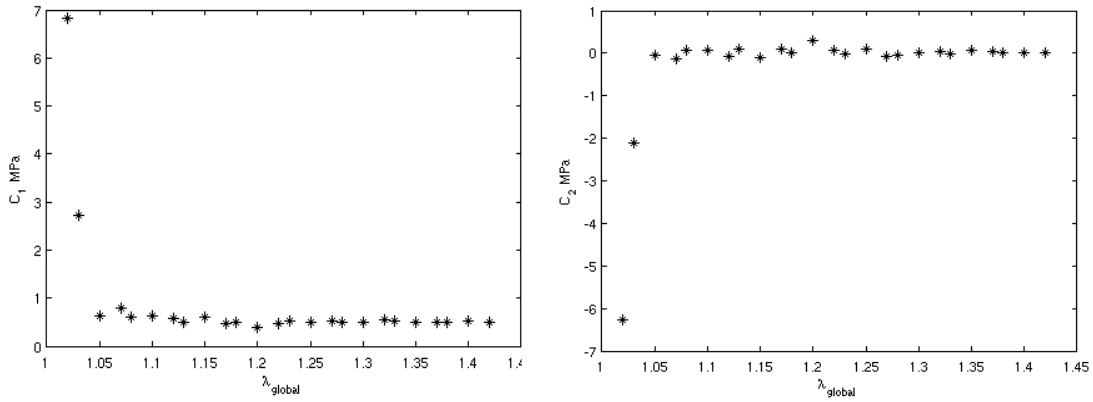

(a) (b)

Figure 10 : Identification of the material parameters (a) $C_{1\,;}$ (b) C_2

Table captions:

Tab. 1: Material formulation (phr) and mechanical properties

Components	NR
Rubber	100
Zinc oxide	9.85
Oil	3
Carbon black	34
Sulphur	3
Stearic acid	3
Antioxidant	2
Accelerators	4
Density	1.13
Shore A hardness	58
Stress at break (MPa)	22.9
Elongation at failure %	635

Tab. 1 : Material formulation (parts per hundred rubber) and mechanical properties